Discrete formulation of envelope correlation coefficient for faster analysis in MIMO antenna systems

Formulación discreta del coeficiente de correlación de envolvente para análisis más rápidos en sistemas de antenas MIMO

Fritz-Andrade Erik
Centro de Investigación y de Estudios Avanzados, CINVESTAV
Instituto Politécnico Nacional
Ingeniería Eléctrica, Comunicaciones
E-mail: erik.fritz@cinvestav.mx
https://orcid.org/0000-0002-5392-8238

Pérez-Miguel Ángel
Centro de Investigación y de Estudios Avanzados, CINVESTAV
Instituto Politécnico Nacional
Ingeniería Eléctrica, Comunicaciones
E-mail: aperezmi@cinvestav.mx
https://orcid.org/0000-0003-4349-0700

Tirado-Méndez José Alfredo
Instituto Politécnico Nacional
E-mail: jtiradom@ipn.mx
https://orcid.org/0000-0002-3288-4416

Vásquez-Toledo Luis Alberto
UAM-Iztapalapa
Departamento Eléctrico
E-mail: lvasquezt@xanum.uam.mx
https://orcid.org/0000-0001-9276-4988

Marcelín-Jiménez Ricardo
UAM-Iztapalapa
Departamento Eléctrico
E-mail: calu@xanum.uam.mx
https://orcid.org/0000-0002-5355-5830

Rodríguez-Colina Enrique
UAM-Iztapalapa
Departamento Eléctrico
E-mail: erod@xanum.uam.mx
https://orcid.org/0000-0003-1696-3349

Pascoe-Chalke Michael
UAM-Iztapalapa
Departamento Eléctrico
E-mail: mpascoe@xanum.uam.mx
https://orcid.org/0000-0003-4057-8715

Abstract

In this paper, an easy-to-program mathematical expression to compute the Envelope Correlation Coefficient (*ECC*) between two antennas by using their radiated electric fields at the far-field region is derived. The main advantage of the resulting algorithm is its higher speed to obtain results compared to those used in commercial software. This novel approach presents a discrete equation that can be employed after obtaining the electric field in spherical coordinates by computer simulations. Thus, another alternative arises to report this metric for low or high radiation efficiency antennas, instead of the less accurate S-parameter-based equation, which does not ensure high accuracy when low radiation efficiency antennas are under study. A comparison between the presented algorithm and the results given by commercial software is shown and discussed, in which is clearly observed that the results are greatly convergent, but with the advantage of achieving a lesser time uting period by the proposed method.
Keywords: Spatial diversity, envelope correlation coefficient, multiple-input-multiple-output (MIMO) systems.

Resumen

En este artículo se presenta la derivación fácil de una expresión matemática de programas para calcular el Coeficiente de Correlación de Envolvente (ECC, por sus siglas en inglés) entre dos antenas, después de obtener las expresiones de campo eléctrico en la región de campo lejano. La principal ventaja del algoritmo resultante es su alta rapidez para obtener resultados comparando el proceso con las herramientas que utilizan los softwares comerciales. Esta novedosa representación proporciona una ecuación discreta que se puede emplear después de obtener el campo eléctrico en coordenadas esféricas mediante procesos de simulación computacional. Por lo tanto, se obtiene otra alternativa eficiente para repostar el ECC tanto en antenas con baja o alta eficiencia de radiación, en lugar de utilizar una ecuación menos precisa basada en los parámetros S, la cual no asegura una alta precisión cuando se utilizan antenas con baja eficiencia de radiación. En el artículo se presenta una comparación de resultados obtenidos mediante el algoritmo propuesto con los resultados obtenidos mediante software comercial, observándose una gran convergencia de valores, pero con la ventaja de que los tiempos de simulación son marcadamente menores cuando se utiliza el método desarrollado en esta investigación.
Descriptores: Diversidad espacial, coeficiente de correlación de envolvente, sistemas de múltiple entrada-múltiple salida.

Introduction

The rise of 5G wireless standard boosts the interest for developing compliant transceivers, motivated by their appealing potential characteristics: increased electromagnetic compatibility, more reliability, more integration with other communication systems, wide bandwidths, low latency, among others (Kimery, 2017). Such features can be achieved by exploiting 4G legacy technology, particularly multi-antenna schemes, e.g. multiple-input multiple-output (MIMO) communications, beamforming arrays, space division multiple access (SDMA), and so on. However, the usage of multiple antennas on both sides of the channel implies the mandatory reduction of the electromagnetic mutual coupling among radiators and the measurement of several propagation-related parameters featured by the antennas. To maximize the capacity of the communications channel, each element of the array should receive a signal completely uncorrelated to the remaining signals arriving at the rest of the radiators. Thence, a metric to measure as straightforwardly as possible this phenomenon is needed.

A widespread metric found in the state-of-the-art to characterize the diversity performance of a pair of antennas is the Envelope Correlation Coefficient (ECC or p_{eij}). An adequate determination of the ECC is relevant to Research and Development (R&D) projects because it gives certainty about the behavior of a system of antennas, by establishing a measurable and a comparison point between prototypes. If the ECC is low, the proposed design is considered as "appropriate for MIMO applications". Otherwise, mutual coupling reduction techniques become the kernel of the work, and their efficacy is proved by measuring the ECC before and after the implantation of the decoupling method. Thence, a novel mutual-coupling-reduction technique is publicized. Therefore, ECC and other multi-antenna parameters are fundamental to grant certainty to microwave and mm-wave related investigations.

However, the calculation and measurement of the ECC is a devious task. The so-called "exact method" or "far-field method" (Choi, 2019) needs the integration of the radiated electric field ($\vec{E}$) of both antennas, measured on the far region, for every frequency over the bandwidth of interest. Therefore, specialized equipment and long measurement sessions are needed.

In the literature about RF and microwave theory and techniques, several alternatives have emerged to ease the computation of ECC, by simplifying Eq. (1) through many assumptions, some of them are not valid for every case. If simplified equations are applied to compute the ECC, inequitable comparisons between characterized prototypes may occur. As well, if two an-tenna models are characterized by using different ECC equations, which follow distinct assumptions, an inequitable confrontation could arise. In both cases, wrong conclusions may be drawn, and a methodological error could be made.

In this paper, an easy-to-program algorithm that allows computing the ECC by means of their simulated $\vec{E}$ fields on the far-field region (also called Fraunhofer region) is developed and presented. This procedure permits to reduce the complexity of simulation of the ECC value over a certain bandwidth without loss of generality. For demonstration purposes, the novel algorithm is applied to two patch antenna arrays, of two elements each, intended for MIMO applications. The results are compared to those got by computer analysis obtained by two commercial electromagnetic simulation applications. It is shown that the presented algorithm calculates the ECC up to 77 times faster than the commercial tools with great convergence among results.

State-of-the-art of calculation of the ECC

The correlation coefficients are used in the microwave and mm-wave literature to quantify the similarity of two communication channels (Chen, 2015a), by mathematically relating the incoming signals at the ports of a MIMO antenna (Ying, 2015). Mainly, three metrics are used to measure the correlation: power correlation coefficient, signal correlation coefficient, and envelope correlation coefficient (ECC) (Chen, 2015b; Rahmat, 2005). The latter is the most popular among antenna designers because it allows quantifying the orthogonality between radiation patterns of two antennas in the vicinity (Clauzier, 2015; Sharawi, 2017). The ECC decreases inversely proportional to the isolation among two ports, thence, if two nearby antennas are adequately decoupled, the ECC is expected to below (Wang, 2016). Recent literature considers ECC = 0.5 as an adequate limit for MIMO systems, in particular, for antenna arrays used on cellular telephony (Ying, 2015; Tsouslos, 2006).

The far-field radiation pattern method (Choi, 2019) to calculate the ECC utilizes the radiated field components from the i-th and j-th antenna following (1):

$$\rho_{e_{ij}} = \frac{\left| \iint_{4\pi} \left[\langle \vec{E_i}(\theta,\phi), \vec{E_j}(\theta,\phi) \rangle \right] d\Omega \right|^2}{\iint_{4\pi} \left| \vec{E_i}(\theta,\phi) \right|^2 d\Omega \iint_{4\pi} \left| \vec{E_j}(\theta,\phi) \right|^2 d\Omega} \tag{1}$$

Where:

$\vec{E_k}(\theta,\phi)$ = complex vector function that describes the k-th 3D radiation pattern at the Fraunhofer zone

$\langle,\rangle$ = Hermitian product
$d\Omega$ = the solid angle differential

The integration over the complete sphere of the electric field radiated on the far-field region from the antennas, for all the frequencies over the whole operational bandwidth can be an expensive and cumbersome task since all values must be measured inside an appropriate facility. Several more cost-effective alternatives to compute the *ECC* has been developed in order to avoid this exact but devious method, as shown below.

For instance, (2) describes the same coefficient by applying the cross-polarization ratio (*XPR*), the components on θ and φ of the polarized electric field (*Ek* (Ω)), and the average power of the vertical P_θ and horizontal P_ϕ components (Andersen, 2003). However, its use is restricted to describe the performance of communication links in Rayleigh-fading channels (Ying, 2015).

$$\rho_{e_{ij}} = \frac{\left|\oint \left[E_i(\theta)E_j^*(\theta)+E_i(\phi)E_j^*(\phi)\right]d\Omega\right|^2}{\left|\oint\left[E_i(\theta)E_i^*(\theta)P_\theta XPR + E_i(\phi)E_i^*(\phi)P_\phi\right]d\Omega \oint\left[E_j(\theta)E_j^*(\theta)P_\theta XPR + E_j(\phi)E_j^*(\phi)P_\phi\right]d\Omega\right|}$$
(2)

Blanch, *et al.* (2003) derived (3), based on the scattering parameters of high-efficiency single-mode antenna systems. It does not require the measurement of the radiation pattern of the antennas under evaluation and it provides a clearer insight into the mutual coupling of two antenna ports. Its simplicity to evaluate over any given bandwidth induced its quick acceptance among the antenna designers.

$$\rho_{e_{ij}} = \frac{\left|\sum_{n=1}^N S_{ni}^* S_{nj}\right|^2}{\left(1-\sum_{n=1}^N |S_{ni}|^2\right)\left(1-\sum_{n=1}^N |S_{nj}|^2\right)}$$
(3)

However, some important drawbacks have been pointed out:

1. Equation (3) does not consider the total efficiency of the radiators, causing a strong deviation between the results obtained from it and from (1) when low-efficient radiators are evaluated (Sharawi, 2017). An expression that sets a lower limit or "guaranteed coefficient" was developed in (Hallbjorner, 2005), but large uncertainties are presented when the total efficiency is low, causing that the expression does not provide useful information for those cases.
2. Equation (3) can be only applied to lossless antennas, which is not the case for many applications. In (Li, 2013), a method based on the insertion of a shunt or series resistor, which represents the dielectric and conductor losses in the equivalent circuit of the an-

tenna, was proposed. Simulations and measurements proved the high convergence of the technique compared to the far-field method, but its intricate procedure and difficulty to identify the appropriate equivalent circuit for every antenna complicate its application. Besides, it is only applicable for single-mode antennas that exhibit strong currents near the excitation port (Li, 2013).

An even more complex method using the cross-correlation Green's function was elaborated in Antar (2015) and combined with the finite-difference time-domain method in (Srivastava, 2017), obtaining upstanding results, but at the expense of embroiling, even more, the calculation of the correlation coefficient. Recently, a method based on Spherical Near Field measurements was presented in (Cornelius, 2017), but its adoption has been not widely accepted till the date (Alieldin, 2018).

There is a direct trade-off between accuracy and complexity of the calculation method; moreover, the antenna array under study must meet the specified conditions which justify the simplifications of the *ECC* calculation, otherwise, the calculated value may lack physical sense.

Sᴛᴀᴛᴇ-ᴏꜰ-ᴛʜᴇ-ᴀʀᴛ ᴏꜰ ᴄᴏᴍᴘᴜᴛᴇʀ-ᴀssɪsᴛᴇᴅ ᴄᴀʟᴄᴜʟᴀᴛɪᴏɴ ᴏꜰ ECC

ANSYS HFSS and CST Studio Suite are two widely accepted programs among investigators focused on R&D of microwave and mm-wave components and devices. Both applications can compute essential data involved in the design process of antennas, filters, transmission lines, and so on. Their solvers are based on the finite-element method (FEM) and the FDTD method, respectively. They can calculate relevant parameters, such as input impedance, the magnitude of radiated fields, attenuation, surface currents, among others. The most recent versions of both applications offer more specialized results obtained by post-processing, but they must be managed by the user after their solvers converge. Amidst these semiautomatic options, the calculation of multiport parameters is found.

HFSS contains a subroutine, referred to as "toolkit", which returns the calculated *ECC* and diversity gain of a solved array of antennas but does not clarify the computing procedure (ANSYS, 2017). Such calculations must be performed for every frequency. Besides, this program does not offer any other alternative to compute the *ECC*.

On the opposite side, CST Studio Suite calculates by default the *ECC* between antennas using the scattering matrix method of (3) and offers a post-processing tool

that calculates the coefficient using (2). Both methods of *ECC* evaluation can be performed over a frequency interval, without the necessity of setting monitors for each frequency, and their results are coincident if and only if three conditions are met:

1. The Gaussian distributions which describe the average power on vertical and horizontal components (P_θ and P_ϕ respectively) are equal ($P_\theta = P_\phi = 1$).
2. Cross-polarization radiation is zero ($XPR = 0$ dB).
3. The model under study is lossless (Computer Simulation Technology AG, 2010).

Both HFSS and CST offer the radiated E-field values of any simulated prototype in the Fraunhofer region, conveniently as real and imaginary parts over the θ and ϕ directions; however, on HFSS a Setup must be established for every frequency, or Discrete sweep must be performed, and a monitor must be set on CST per frequency of calculation. Therefore, if the interval of frequencies is extended, as in wideband and UWB antennas, the calculation time and required computational resources grow.

MATHEMATICAL DERIVATION OF THE NEW METHOD

The expression appearing in (Blanch, 2003) to determine the envelope correlation coefficient of two antennas by means of their radiated electric fields in the far-field region is shown in this paper as (1). $\vec{E_k}(\theta, \phi)$ is a complex vector function that describes the 3D radiation pattern of the antenna excited by the k-th port, and its θ and ϕ components are denoted by $E_{k,\theta}(\theta, \phi)$ and , respectively. Since $\vec{E_k}$ is a complex vector function, it can be described for every point in the far-field region by four components, as given in Eq. (4). These four components are available in simulated results from commercial solvers.

$$\vec{E_k}(\theta,\phi) = [\Re\{E_{k,\theta}(\theta,\phi)\} + j\Im\{E_{k,\theta}(\theta,\phi)\}]\hat{\theta} + [\Re\{E_{k,\theta}(\theta,\phi)\} + j\Im\{E_{k,\theta}(\theta,\phi)\}]\hat{\phi} \tag{4}$$

The Hermitian product of two different complex vector functions is calculated using Equation (5):

$$\langle \vec{F_i}(\theta,\phi), \vec{F_k}(\theta,\phi) \rangle = F_{i,\theta}(\theta,\phi)F_{k,\theta}^*(\theta,\phi) + F_{i,\phi}(\theta,\phi)F_{k,\phi}^*(\theta,\phi) \tag{5}$$

In which * denotes the complex conjugate function. It must be remarked that the squared modulus of a complex vector function can be expressed as a Hermitian product, as displayed in (6).

$$\left|\vec{F_k}(\theta,\phi)\right|^2 = \langle \vec{F_k}(\theta,\phi), \vec{F_k}(\theta,\phi) \rangle \tag{6}$$

The Hermitian product of a function $\vec{F_k}$ with itself can be also written as (7) in terms of the real and imaginary parts of the results of (5):

$$\langle \vec{F_k}(\theta,\phi), \vec{F_k}(\theta,\phi) \rangle = \Re\{F_{k,\theta}(\theta,\phi)\}^2 + \Im\{F_{k,\theta}(\theta,\phi)\}^2 + \Re\{F_{k,\phi}(\theta,\phi)\}^2 + \Im\{F_{k,\phi}(\theta,\phi)\}^2 \tag{7}$$

Thence, (1) can be written in the more compact fashion of (8):

$$\rho_{e_{ij}} = \frac{|B_{ij}|^2}{B_{ii}B_{jj}} \tag{8}$$

by defining B_{ij} as (9):

$$B_{ij} = \iint_{4\pi} [\langle \vec{E_i}(\theta,\phi), \vec{E_j}(\theta,\phi) \rangle] \, d\Omega \tag{9}$$

Equation (9) can be used to represent the denominator of (8) by substituting i for j and vice versa. By defining the integration limits and substituting the differential $d\Omega = \sin\theta \, d\theta \, d\phi$ (9) can be rewritten as (10):

$$B_{ij} = \int_0^{2\pi} \int_0^\pi [\langle \vec{E_i}(\theta,\phi), \vec{E_j}(\theta,\phi) \rangle] \sin\theta \, d\theta d\phi \tag{10}$$

To apply the current method in a measurement or simulation process, (10) must be discretized since both simulated and measured electric fields radiated from an assembly of antennas are always a finite number of samples. For the most general case, closed-form expressions for the radiated field from an assembly of antennas are not always available; therefore, the integrations on (10) cannot be performed analytically. Following the procedure explained by Balanis (2001), section 2.7, a series approximation of (10) can be deduced as (11):

$$B_{ij} \cong \sum_{m=1}^M \sum_{n=1}^N [\langle \vec{F_i}(\theta_n,\phi_m), \vec{F_j}(\theta_n,\phi_m) \rangle] \sin\theta_n \, \Delta\theta_n\Delta\phi_m \tag{11}$$

Where N uniform partitions of θ are obtained by means of (12):

$$\Delta\theta_n = \frac{\pi}{N} \tag{12}$$

Making the discreet variable θ_n equals to:

$$\theta_n = n(\Delta\theta_n) = n\frac{\pi}{N} \tag{13}$$

Similarly, M uniform partitions of ϕ are obtained using (14):

$$\Delta\phi_m = \frac{2\pi}{M} \tag{14}$$

Obtaining a discrete variable ϕ_m:

$$\phi_m = m(\Delta\phi) = m\left(\frac{2\pi}{M}\right) \tag{15}$$

By substituting (12-15) in (11), the approximation of B_{ij} is given by:

$$B_{ij} \cong \frac{2\pi^2}{NM} \sum_{m=1}^{M} \sum_{n=1}^{N} \left[\langle \vec{F_i}(\theta_n, \phi_m), \vec{F_j}(\theta_n, \phi_m)\rangle\right] \sin\theta_n \tag{16}$$

Substituting (16) in (6) in terms of the electric fields, the Envelope Correlation Coefficient can be approximated by using (17):

$$\rho_{e_{ij}} \cong \frac{\left|\sum_{m=1}^{M}\sum_{n=1}^{N}\left[\langle\vec{E_i}(\theta_n,\phi_m),\vec{E_j}(\theta_n,\phi_m)\rangle\right]\sin\theta_n\right|^2}{\sum_{m=1}^{M}\sum_{n=1}^{N}\left[\langle\vec{E_i}(\theta_n,\phi_m),\vec{E_i}(\theta_n,\phi_m)\rangle\right]\sin\theta_n \sum_{m=1}^{M}\sum_{n=1}^{N}\left[\langle\vec{E_j}(\theta_n,\phi_m),\vec{E_j}(\theta_n,\phi_m)\rangle\right]\sin\theta_n} \tag{17}$$

Applying (3-5), the components of functions $\vec{E_k}$ defined over θ_n and ϕ_m coordinates can be expressed by using (18-19):

$$\rho_{e_{ij}} \cong \frac{\left|\sum_{m=1}^{M}\sum_{n=1}^{N}\left[E_{i,\theta}(\theta_n,\phi_m)E_{j,\theta}^*(\theta_n,\phi_m) + E_{i,\phi}(\theta_n,\phi_m)E_{j,\phi}^*(\theta_n,\phi_m)\right]\sin\theta_n\right|^2}{\sum_{m=1}^{M}\sum_{n=1}^{N}A_i(\theta_n,\phi_m)\sin\theta_n \sum_{m=1}^{M}\sum_{n=1}^{N}A_j(\theta_n,\phi_m)\sin\theta_n} \tag{18}$$

Where:

$$A_k\left(\theta_n,\phi_m\right) = \Re\left\{E_{k,\theta}\left(\theta_n,\phi_m\right)\right\}^2 + \Im\left\{E_{k,\theta}\left(\theta_n,\phi_m\right)\right\}^2$$

$$+ \Re\left\{E_{k,\phi}\left(\theta_n,\phi_m\right)\right\}^2 + \Im\left\{E_{k,\phi}\left(\theta_n,\phi_m\right)\right\}^2 \tag{19}$$

The calculation method exposed here features more application generality than many of the procedures listed on the Introduction section, because it is not subject to radiation efficiency, total efficiency, port matching, and other characteristics of the antennas under test (AUT). This procedure establishes, directly the interaction of both radiated electric fields, instead of deducing it from the relations among other parameters, as other methods of calculation do (ANSYS, 2017) (Computer Simulation Technology AG, 2010).

COMPARING RESULTS TO COMMERCIAL ELECTROMAGNETIC SIMULATORS

In order to prove the accuracy of the approximation made by Equations (18-19), a comparison of the results obtained by the presented numerical method, FDTD and FEM-solver solutions was performed. For demonstration purposes, two arrays consisting of two microstrip patch antennas were designed in HFSS 15 and CST Studio Suite 2016, on a Rogers RT/duroid 5880 substrate with thickness $h = 1.27$ mm, relative permittivity $\varepsilon_r = 2.2$ and tan $\delta = 0.0004$, as pictured on Figure 1, tuned to a center frequency of 2.45 GHz. Model "a" or "orthogonal" consists of two identical and independent patches placed perpendicularly one to each other, driven by a coplanar microstrip; model "b" or "copolar" places such patches collinear to each other, excited by means of an SMA connector. Microstrip patch antennas were selected since, as stated before, Eq. (3) is restricted to high-efficiency radiators, and this equation is going to be considered in the total analysis.
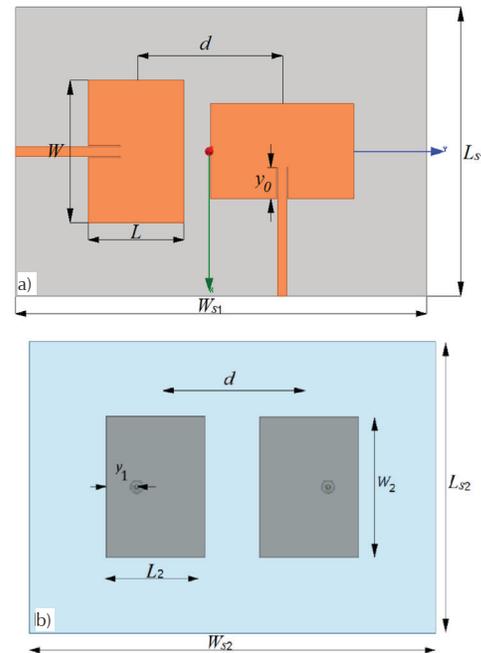
Figure 1. a) Model of orthogonal antennas and b) Model of collinear (copolar) antennas used along in this paper. Dimensions listed in Table 1

By using the classic microstrip patch antenna design and following the equations given in (Garg, 2001), the dimensions of the AUT were found and tuned by using the commercial electromagnetic simulation programs under test. Optimal dimensions are listed in Table 1, and the simulated S-parameters are shown in Figure 2. This figure also shows that the -10 dB impedance band-

width of each element is approximately 30 MHz, from 2.43 to 2.46 GHz.

Table 1. Dimensions of antenna arrays pictured on Figure 1

Dimension	Magnitude [mm]
d	61.1825
h	1.27
L_1	40.1
L_2	39.5
L_{s1}	101.2825
L_{s2}	118.22
W_1	60.15
W_2	59.25
W_{s1}	162.465
W_{s2}	161.95
y_0	13.32
y_1	12.25

In order to create comparable simulation conditions, the simulated results from both programs needed to be as similar as possible. This condition is almost accomplished for all parameters in both configurations, ex-

cept for the S_{22} parameter, shown in Figure 2c, which magnitude diverges from that obtained with HFSS for the orthogonal configuration. To assure these results, every simulation on this paper was performed using a PC with 48 GB RAM, dual-core Intel Xeon processor with a 2.4 GHz internal clock. In HFSS, the convergence criterion (given by the parameter "Maximum Delta S") was established on 0.015. In CST, the convergence criterion is influenced by the number of hexahedral cells per wavelength, established as 40, and is determined by the reflected wave "accuracy", which was determined to be −40 dB. These conditions allowed obtaining an elevated similitude of the calculated S-parameters, as Figure 3 shows. This figure presents the high similarity of the real and imaginary parts of the scattering coefficients obtained from both EM simulators.

Figure 4 shows that the radiation efficiency and the total efficiency of the AUT, calculated by CST. These parameters exceed 80 % over their impedance bandwidth. Therefore, the use of Eq. (3) is also valid for these models.
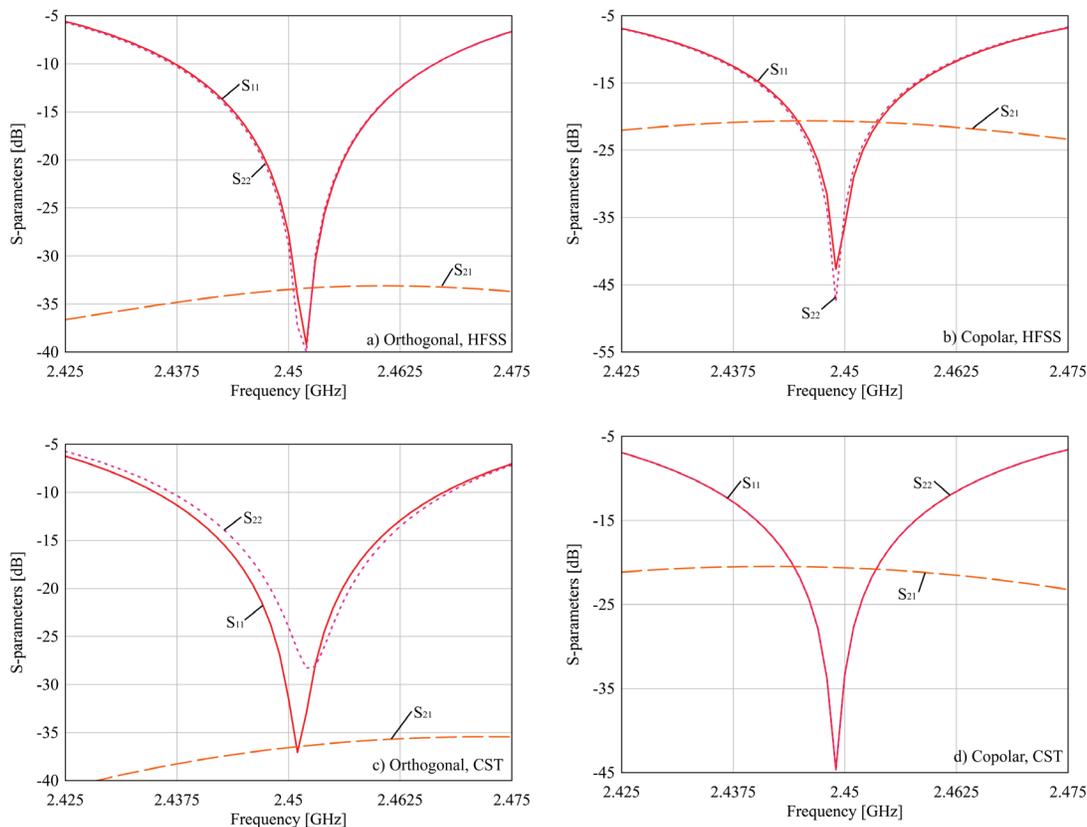
Figure 2. Magnitudes of the S parameters (in dB), calculated for the models "a" and "b" described on Figure 1, using HFSS and CST Studio Suite
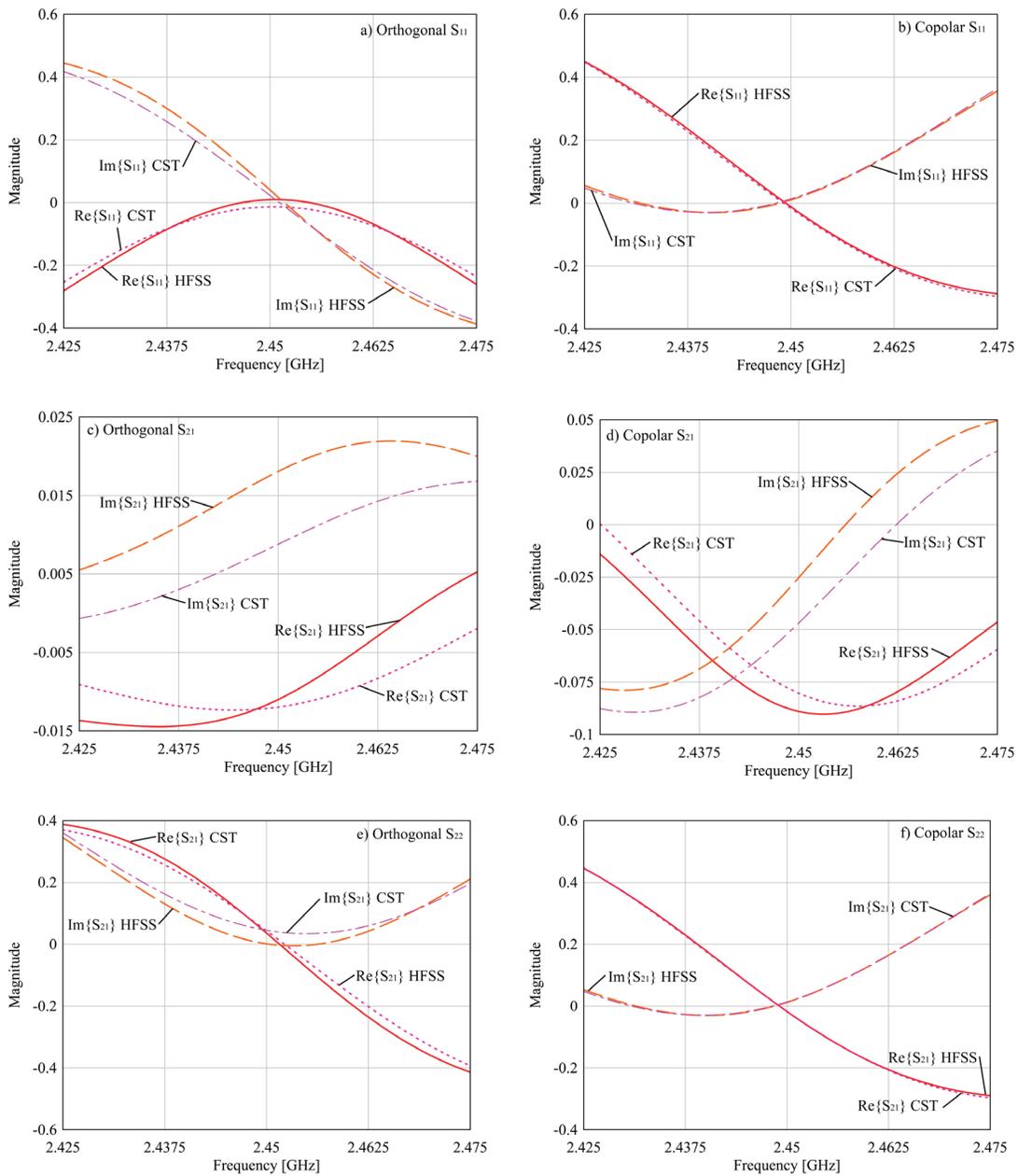
Figure 3. Comparison of the magnitudes of the real and imaginary parts of the scattering parameters for models orthogonal and copolar described on Figure 1, calculated by HFSS and CST Studio Suite
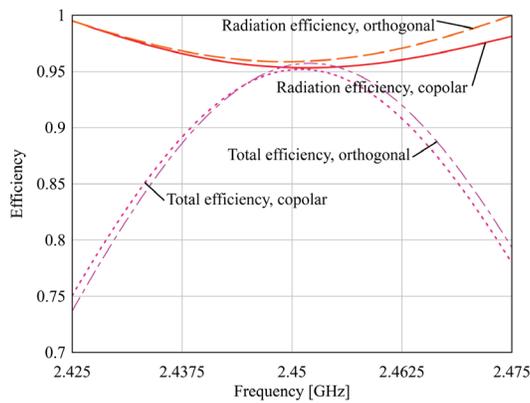
Figure 4. Radiation efficiency and total efficiency *vs* frequency of the antenna arrays depicted on Figure 1
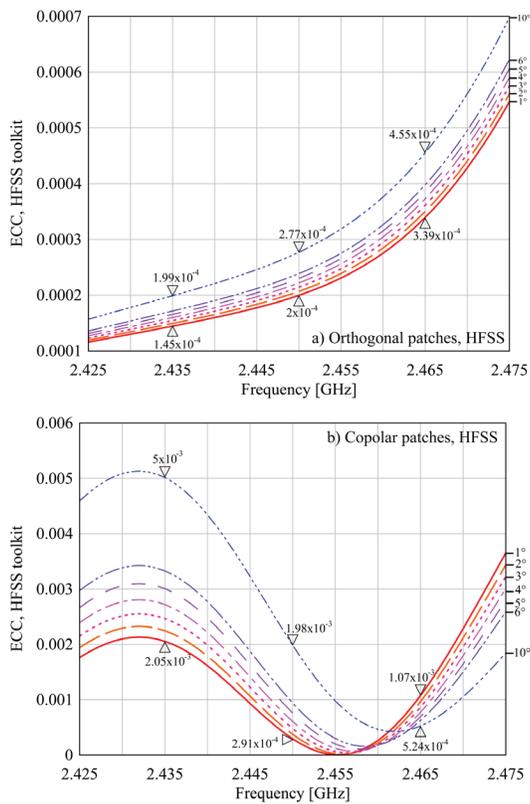
Figure 5. *ECC* curves calculated for a) Orthogonal and b) Copolar models by means of the HFSS toolkit

For the purposes of this study, the spatial sampling step, over θ and ϕ coordinates, is called "angular resolution". An angular resolution of 1 means that the spatial samples were registered every degree all over the infinite sphere, and so on.

Figure 5 shows the calculation of *ECC* every 1 MHz over the 2.425 – 2.475 GHz interval, obtained by the HFSS toolkit for both models of the AUT, using angular resolutions of 1°, 2°, 3°, 4°, 5°, 6° y 10°. As determined in

recent literature, both arrays are acceptable to be used on MIMO communication, because the *ECC* values are considerably lesser than 0.5. Figure 5a, reveals that the *ECC* values for the orthogonal array exhibit more convergence than for the copolar array. A likely reason is that this is caused by the elevated mutual coupling between copolar patches, as S_{21} reveals in Figure 2. The trend shown in Figure 5 allows deducing that the accuracy of *ECC* calculation grows when the spatial sample size is reduced. However, the simulation time is increased, as Table 2 shows.

Table 2. Relation between angular resolution and simulation time exhibited by HFSS toolkit and CST post-processing tool, for orthogonal and copolar arrays

Angular resolution [°]	No. of samples	HFSS Simulation time [s]		CST Simulation time [s]	
		Orthogonal array	Copolar array	Orthogonal array	Copolar array
1	64800	1887	2015	886	910
2	32400	455	478	268	306
3	7200	205	218	160	186
4	4050	129	133	115	124
5	2592	83	86	97	110
6	1800	62	66	85	86
10	648	30	33	65	69

The results of applying the post-processing tool of CST to compute *ECC*, considering $P_{\theta} = P_{\phi} = 1$ and $XPR = 0$ dB, are shown in Figure 6, which induces to conclude that this method is not sensible to the angular resolution. By examining Table 2, it is shown that HFSS doubles the simulation time of CST for similar conditions.

The complex-valued electric fields on the Fraunhofer region for both models were obtained by means of HFSS and CST, and (18-19) were applied to obtain the *ECC*. The proposed method was programmed on C language, due to its high efficiency on the dynamic memory allocation, compared to Matlab or Python. The algorithm is described on Appendix A. For each angular resolution, the fields on the far region were exported, on the band of 2.425-2.475 GHz, with a step width of 1 MHz, corresponding to 51 points. On Figure 7, the *ECC* curves calculated by using (18-19), for different angular resolutions using the $\bar{E}$ field obtained by HFSS are shown. Figure 8 pictures the values of *ECC* calculated by the novel method, by using the fields delivered by CST for distinct angular resolutions.

As observed in Figures 7 and 8, the angular resolution has more impact on the performance of the proposed method when using the $\bar{E}$ field calculated by HFSS, than when using the ones from CST. For the same model, the variation of the magnitude of *ECC* varies more by employing the HFSS fields when the angular resolution is modified. Therefore, it is necessary to reduce the angular step in HFSS as much as possible, but this must
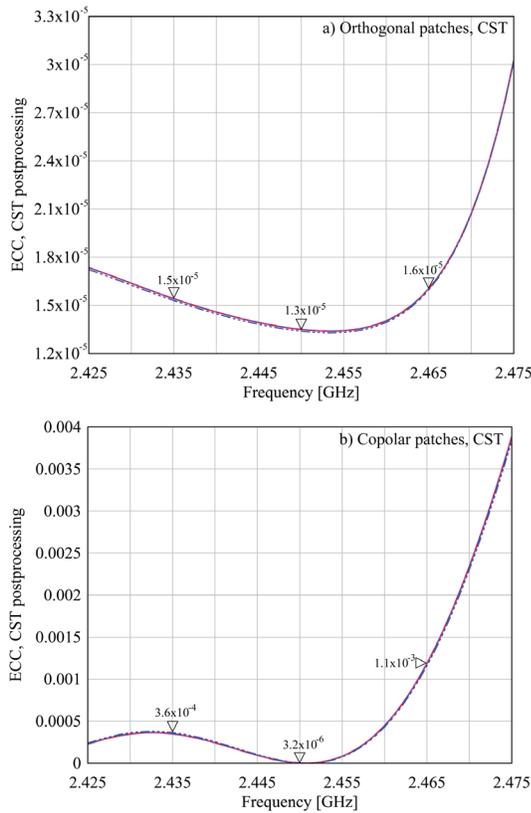
Figure 6. *ECC* curves calculated for a) Orthogonal and b) Copolar models by means of the CST post-processing tool

Table 3. Relation between angular resolution and simulation time exhibited by the proposed method

Angular resolution [°]	Proposed method, HFSS fields, 1°, orthogonal [s]	Proposed method, HFSS fields, 1°, copolar [s]	Proposed method, CST fields, 1°, orthogonal [s]	Proposed method, CST fields, 1°, copolar [s]
1	52.89	51.55	69	68.52
2	13.11	12.67	23	17.32
3	5.965	5.753	8	7.863
4	3.577	3.271	4.606	4.568
5	2.266	2.236	3.092	3.053
6	1.562	1.58	2.214	2.197
10	0.7137	0.6653	0.921	0.895
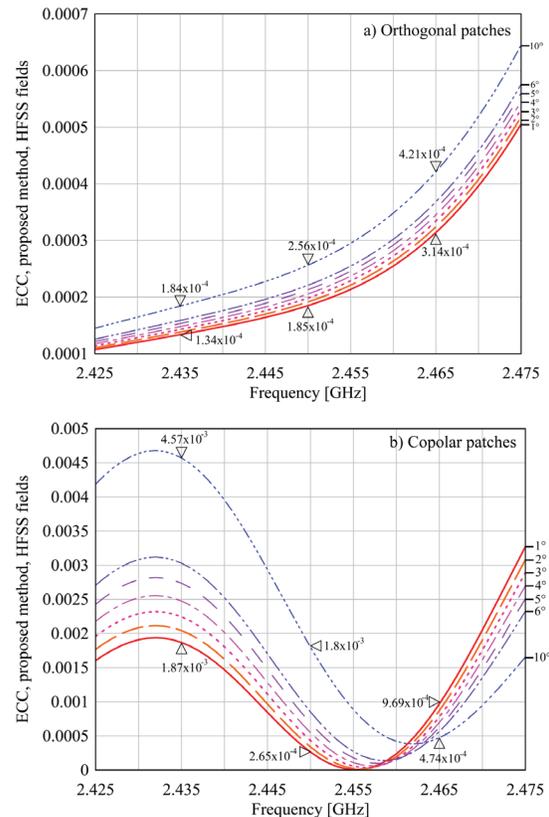
Figure 7. Calculated *ECC* values depending on the angular resolution, using (18-19) and HFSS for the a) Orthogonal and the b) Copolar models

be compromised to the simulation time. Simulation time grows as angular resolution tends to 1°, as could be expected.

As Table 2 reveals, HFSS exhibits the largest simulation time, which doubles CST calculation time for the angular resolution of 1°. On the other hand, the proposed method shows little sensibility to the geometry of the AUT, unlike is observed on commercial solvers. Moreover, as seen by comparing the results displayed in Table 2 and Table 3, the proposed algorithm is between 39 and 49 times faster than the HFSS toolkit, and 12 to 13 times compared to CST postprocessing tool on the calculation time. It is remarked that the simulation time of the proposed procedure becomes more competitive to CST post-processing tool as the spatial step is enlarged: for an angular resolution of 4°, the proposed algorithm is 27 times faster than CST semiautomatic tool, but when the resolution is changed to 10°, the proposed algorithm gets the *ECC* results 77 times faster than CST.

The comparison of applying the proposed algorithm, HFSS, and CST post-processing tools, and the S-parameters method described by Eq. (3), is found in Figure 9. It is revealed that the algorithm calculates

very similar values to the commercial semiautomatic tools when their respective computed $\bar{E}$ fields are used. This fact is demonstrated by the high similitude between the calculated curves from this novel procedure, and the values calculated by HFSS when its electric
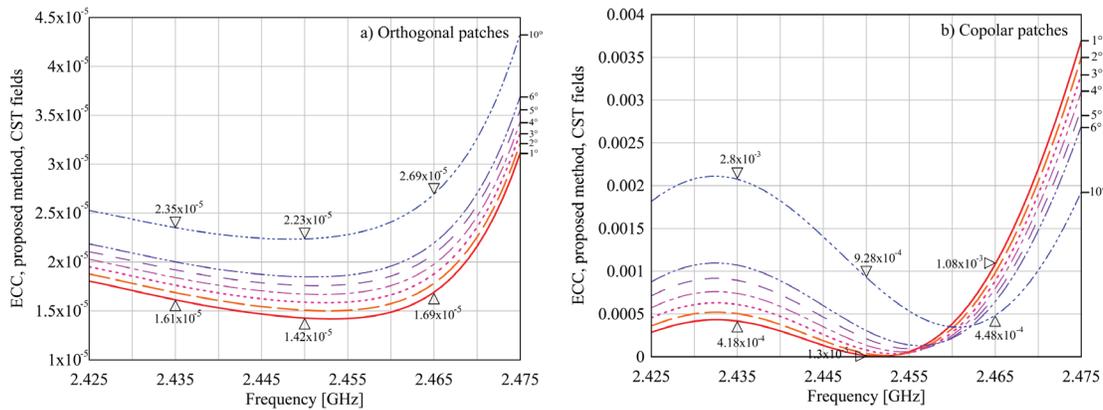
Figure 8. Calculated *ECC* values depending on the angular resolution, using (18-19), and CST for the a) Orthogonal and the b) Copolar models

fields are the input variables for the algorithm. As well, when the $\vec{E}$ fields from CST are applied to this novel procedure, their obtained values are very close to those computed by the post-processing option from CST. It is also noted that there is a discrepancy between the values calculated from data proceeding from HFSS and CST for the orthogonal array. However, this divergence is not bigger than 2×10^{-4} at the design frequency. This may be due to the intrinsic differences between FEM and FDTD methods. For a clearer understanding of the obtained results, the curves shown in Figure 9a and b

were split into Figure 9c, d, e, f, g, h, i, and j. From these last figures, it is observed that, at the design frequency, the convergence of the results for the different methods and the algorithm proposed in this work is very high, showing two small differences in Figure 9e and Figure 9i, where the proposed procedure presents a small variation compared to the results obtained by HFSS and CST when the S-parameter method is employed. However, this variation is not bigger than 2×10^{-4} units, which is negligible compared to 0.5, which is the goal level.

Figure 9. Comparison of *ECC* calculations from different equations and solvers. a) Comparison of all the available methods for the orthogonal patches, b) Comparison of all the available methods for the copolar patches, c) Proposed method *vs* HFSS toolkit on the orthogonal patches, d) Proposed method *vs* HFSS toolkit on the copolar patches, e) Proposed method *vs* (3) from HFSS on orthogonal patches, f) Proposed method *vs* (3) from HFSS on copolar patches, g) Proposed method *vs* CST post-processing tool on the orthogonal patches, h) Proposed method *vs* CST post-processing tool on the copolar patches, i) Proposed method *vs* (3) from CST on orthogonal patches, j) Proposed method *vs* (3) from CST on copolar patches   Keep going...

Continuation.......

Figure 9. Comparison of *ECC* calculations from different equations and solvers. a) Comparison of all the available methods for the orthogonal patches, b) Comparison of all the available methods for the copolar patches, c) Proposed method *vs* HFSS toolkit on the orthogonal patches, d) Proposed method *vs* HFSS toolkit on the copolar patches, e) Proposed method *vs* (3) from HFSS on orthogonal patches, f) Proposed method *vs* (3) from HFSS on copolar patches, g) Proposed method *vs* CST post-processing tool on the orthogonal patches, h) Proposed method *vs* CST post-processing tool on the copolar patches, i) Proposed method *vs* (3) from CST on orthogonal patches, j) Proposed method *vs* (3) from CST on copolar patches   Keep going...

Continuation.......

Figure 9. Comparison of *ECC* calculations from different equations and solvers. a) Comparison of all the available methods for the orthogonal patches, b) Comparison of all the available methods for the copolar patches, c) Proposed method *vs* HFSS toolkit on the orthogonal patches, d) Proposed method *vs* HFSS toolkit on the copolar patches, e) Proposed method *vs* (3) from HFSS on orthogonal patches, f) Proposed method *vs* (3) from HFSS on copolar patches, g) Proposed method *vs* CST post-processing tool on the orthogonal patches, h) Proposed method *vs* CST post-processing tool on the copolar patches, i) Proposed method *vs* (3) from CST on orthogonal patches, j) Proposed method *vs* (3) from CST on copolar patches

CONCLUSIONS

In this paper, an easy to program accurate algorithm to compute the Envelope Correlation Coefficient from the computed radiated electric fields on the Fraunhofer region is proposed. The novel procedure is applied to a study case, obtaining the *ECC* values up to 77 times faster than the commercial software tools without losing any accuracy. The developed algorithm was compared to two of the most used electromagnetic simulator software, and the computing time of the *ECC* is greatly enhanced by several magnitudes. On the other hand, it is demonstrated that this process does not need special care regarding cross-polarization levels, radiation efficiency, or any other factor that can increase the complexity of the calculation of the metric. All these algorithm features are obtained without compromising the exactness of the results. The relative error of the method compared to the other two ones, changed from some percent units when the angular resolution was set to the smallest value, close to 1°, and tends to increase to some percent tens as the angular resolution rises. For example, for HFSS goes from 3 % to 39 % at the center frequency when the angular resolution changes from 2° to 10°, respectively. For CST, considering the same case, the error changes from 6 % to 57 %, taking the same angular resolution.

This procedure is proposed to ease the computation of *ECC*, for the sake of reducing certain methodological errors indicated in this work.

Appendix A

they contain the data for all the samples of the angles θ and ϕ, and for all frequencies, and for each part real and imaginary and component in θ and ϕ.

A set of samples of the matrixes A_i and A_j are assigned to generate two new submatrices, namely E_i and E_j; these submatrices are used to calculate ECC per frequency. In E_i and E_j the value of the electric field per sample is copied. Therefore, each sample contains four components: the real part of theta, the imaginary part of theta, the real part of phi, and the imaginary part of phi. In the computational memory each field component corresponds to a column of the matrix, but five columns are used since all the θ_k values (referred in the flowchart as $\theta[k]$) must be considered as well. The number of rows is given by N and M, consequently, the total of rows of the matrix is $N_T = N \cdot M$.

The auxiliar terms I_1, I_2 and I_3 are scalar variables which save the value of the Hermitian product per row of the matrix $E_{i,j}$. For I_1, the Hermitian product equals to $\langle E_i, E_j \rangle$ and the product is calculated based on Equation (6). The scalar I_2 follows the same principle of I_1, but using the fields of the matrix E_j. The variable I_3 is used for the Hermitian product resulting from the fields of the matrix E_i and E_j, and the result is a purely imaginary number.

Then, the auxiliar terms I_1, I_2 and I_3 must be multiplied by $\sin \theta_k$ and add each contribution to the total summation, and k is an index used to control such addition. As long as $k < N_T$ condition is satisfied, three variables B_{ii}, B_{jj} and B_{ij} save the summation from Equation (16); B_{ii}, B_{jj}, are real-values while B_{ij} is a complex-valued variable.

Finally, ECC at the indicated frequency is calculated by means of B_{ii}, B_{jj} and B_{ij}; such value is saved in an external file. The ECC will be calculated for all frequencies while the condition $i_{freq} < N_{freq}$ is true. When $i_{freq} = N_{freq}$ is met, a vector of ECC versus frequency between the ports i and j is obtained.

References

Alieldin, Y. H. (2018). A 5G MIMO antenna for broadcast and traffic communication topologies based on pseudo inverse synthesis. *IEEE Access*, 6, 65935-65944.

Andersen, R. V. (2003). *Channels, propagation and antennas for mobile communications.* London: The Institution of Electrical Engineers (IET).

ANSYS. (1 de 1 de 2017). www.ansys.com. Recuperado de www.ansys.com

Antar, S. M. (2015). On cross correlation in antenna arrays with applications to spatial diversity and MIMO systems. *IEEE Transactions on Antennas and Propagation*, 63(4), 1798-1810. https://doi.org/10.1109/TAP.2015.2398113

The algorithm to compute ECC in several frequencies is shown in the Figure A-1. The procedure starts initializing the index of the ports i and j to one. ECC is assessed if and only if the i-th port is different of the port j. The number of frequencies N_{freq} in which ECC will be evaluated, and the number of samples N and M of θ and ϕ, respectively, are obtained to establish the dimensions of the data matrix. Then, the data matrices A_i and A_j, associated to the i-th and j-th ports are read;

Balanis, C. A. (2001). *Antenna theory: Analysis and design*. Hoboken. Norwood: Artech House.

Blanch, J. R. (2003). Exact representation of antenna system diversity performance from input parameter description. *Electronics Letters*, 39(9), 705-707.

Chen, X. (2015a). Antenna correlation and its impact on multi-antenna system. *Progress in Electromagnetics Research B, 7*, 563-586. http://dx.doi.org/10.2528/PIERB15012805

Chen, X. (2015b). Antenna correlation and its impact on multi-antenna system. *Progress in Electromagnetic Research B*, 62, 241-253.

Choi, I. N. (2019). Study on mutual coupling reduction technique for MIMO antennas. *IEEE Access, 7*, 563-586.

Clauzier, S. M. (2015). A generalized methodology for obtaining antenna array surface current distributions with optimum cross-correlation performance for MIMO and spatial diversity applications. *IEEE Antennas and Wireless Propagation Letters*, 14, 1451-1454.

Computer Simulation Technology A. G. (1 de 1 de 2010). Recuperado de www.cst.com

Cornelius, A. N. (2017). Calculating envelope correlation coefficient directly from spherical modes spectrum. 11th European Conference on Antennas and Propagation (EUCAP),1-5. Paris: IEEE. Recuperado de http://dx.doi.org/10.23919/EuCAP.2017.7928132

Garg, P. B. (2001). *Microstrip antenna design handbook.* Norwood: Artech House.

Hallbjorner, P. (2005). The significance of radiation efficiencies when using S-parameters to calculate the received signal correlation from two antennas. *IEEE Antennas and Wireless Propagation Letters*, 4, 97-99. https://doi.org/10.1109/LAWP.2005.845913

Kimery, J. (2017). 5G: Is it ready for take off? *Microwave Journal*, 60(12), 24-24.

Li, X. L. (2013). Equivalent circuit based calculation of signal correlation in lossy MIMO antennas. *IEEE Transactions on Antennas and Propagation,* 65(2), 730-740. http://dx.doi.org/10.1109/TAP.2013.2273212

Rahmat, M. M. (2005). Multiport characteristics of a wideband cavity backed annular patch antenna for multipolarization operations. *IEEE Transactions on Antennas and Propagation,* 53(1), 466-474.

Sharawi, A. T. (2017). Correlation coefficient calculations for MIMO antenna systems: a comparative study. *International Journal of Microwave and Wireless Technologies,* 9(10), 1991-2004. https://doi.org/10.1017/S1759078717000903

Srivastava, D. S. (2017). Application of cross-correlation greens function along with FDTD for fast computation of envelope correlation coefficient over wideband for MIMO antennas. *IEEE Transactions on Antennas and Propagation,* 65(2), 730-740. https://ui.adsabs.harvard.edu/link_gateway/2017ITAP...65..730S/doi:10.1109/TAP.2016.2633158

Tsouslos, G. (2006). *MIMO system technology for wireless communications*. Boca Raton: CRC Press.

Wang, Y. C. (2016). Performance of the large-scale adaptive array antennas in the presence of mutual coupling. *IEEE Transactions on Antennas and Propagation,* 64(6), 2236-2245.

Ying, C.-Y. C. (2015). *Handbook of antenna technologies.* Singapore: Springer.